energies

MDPI

Article

A Short-Current Control Method for Constant Frequency Current-Fed Wireless Power Transfer Systems

Yanling Li, Qichang Duan * and Weiyi Li

School of Automation, Chongqing University, 174 Shazheng Street, Shapingba District, Chongqing 400030, China; liyanling1978@gmail.com (Y.L.); 20111301005@cqu.edu.cn (W.L.)

* Correspondence: duanqichang1953@gmail.com; Tel.: +86-23-6510-6188

Academic Editor: Aiguo Patrick Hu

Received: 24 February 2017; Accepted: 20 April 2017; Published: 25 April 2017

Abstract: Frequency drift is a serious problem in Current-Fed Wireless Power Transfer (WPT) systems. When the operating frequency is drifting from the inherent Zero Voltage Switching (ZVS) frequency of resonant network, large short currents will appear and damage the switches. In this paper, an inductance-dampening method is proposed to inhibit short currents and achieve constant-frequency operation. By adding a small auxiliary series inductance in the primary resonant network, short currents are greatly attenuated to a safe level. The operation principle and steady-state analysis of the system are provided. An overlapping time self-regulating circuit is designed to guarantee ZVS running. The range of auxiliary inductances is discussed and its critical value is calculated exactly. The design methodology is described and a design example is presented. Finally, a prototype is built and the experimental results verify the proposed method.

Keywords: frequency drift; current-fed; wireless power transfer; short current; inductance damping

1. Introduction

Wireless Power Transfer (WPT) technology utilizes high frequency magnetic fields to realize energy transfer. This can eliminate the risk of sparks and electrical shocks and make the power transfer process safe and convenient. In recent years, this technology has seen more and more applications in EV charging, biomedical implants and consumer electronics [1–6].

Figure 1 illustrates a typical Current-Fed WPT system. A DC voltage source E_{in} and inductance L_{DC} compose a quasi-current source. A parallel resonant network is used on the primary side. The post-circuit contains a resonant network, rectifier, filter and load. Series, parallel or other types of resonant network can be used on the secondary side of a WPT system.

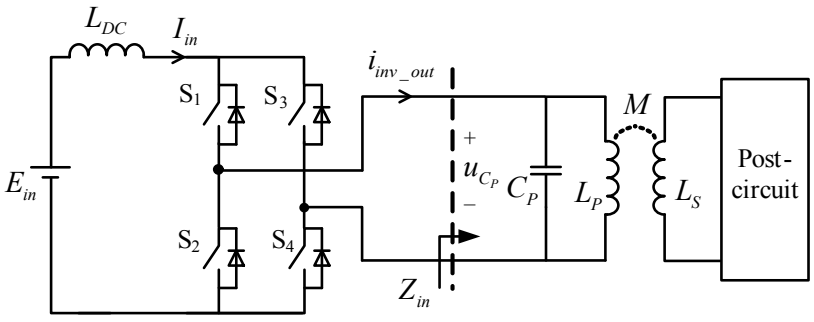

Figure 1. Current-Fed WPT system.

In the above system, the parallel-resonant capacitor C_P has the risk of being shorted by switches. If this happens, a large short current will be generated in the inner loop between the inverter and resonant tank. Mismatch between the Zero Voltage Switching (ZVS) frequency (f_{ZVS}) and operation frequency (f_S) will lead to a short current. The existence of short currents will damage the switching components and greatly increase the risk of breakdown of the whole system. Generally, a short current is a common phenomenon in the topology shown in Figure 2.

One typical type of application circuit is a high step-up converter [7,8]. In these converters, C_P represents the parasitic capacitance of a high turn-ratio transformer. Another typical application circuit is the parallel resonant converter. The Current-Fed WPT system is a parallel resonant converter.

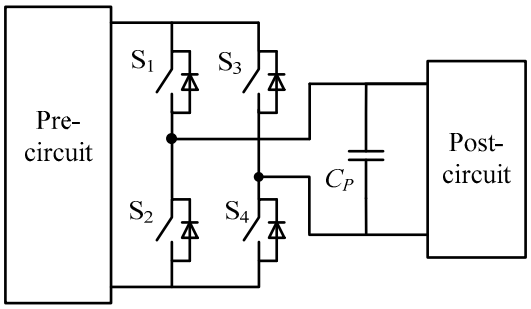

Figure 2. The general topology that can generate short currents.

For a Current-Fed WPT system, frequency drift is an important issue [9,10]. Mutual inductance M and load resistance R_L change dynamically, which means f_{ZVS} cannot be a constant value. Calculation of the ZVS frequency is a complicated and time-consuming process [11,12]. Moreover, real-time load and mutual inductance identification methods also require complex calculations and detection circuits [13,14], so some real-time and simple methods need to be used.

By using a passive zero crossing point detection method such as the ZVS method, operation frequency f_S can keep up with f_{ZVS} in real-time [9,10,15]. However, due to the time lag on the detection route, there exists a mismatch between f_S and f_{ZVS}. Other methods including active frequency tracking [16] and the self-oscillating switching technique [17] are also proposed to reduce short currents. A common property of these methods is that the operating frequency f_S is time-variant in order to track f_{ZVS}. This makes filter design difficult. Another disadvantage of these methods is the frequency-bifurcation phenomenon [12], which will cause a significant decrease of transferred power.

To eliminate short currents and achieve constant frequency operation simultaneously, the classical method utilizes four blocking diodes placed in series with switches to cut off the loops of short current flows [9], which increases the energy losses and costs.

This paper proposes an inductance damping method for Current-Fed WPT systems. The inductance is connected in series with the parallel resonant network. Short currents are suppressed, while no extra switching component needs to be added. All switches of the inverter are ZVS. Most importantly, the method hardly affects the input and output characteristics of the original Current-Fed WPT system. Operation conditions of the system are discussed, including operation frequency, overlapping time and value of L_1. Based on the conditions, a design methodology is proposed to apply the method to traditional Current-Fed WPT systems.

The rest of this paper is organized as follows: Section 2 briefly introduces the mechanism of short current formation in Current-Fed WPT systems. The proposed inductance damping method is elaborated in Section 3. The circuit and its cyclical switching operation are presented. In Section 4, operating conditions governing the use of the proposed method are listed and explained. An overlapping-time self-regulating circuit is described to satisfy the second operation condition in Section 5. Section 6 discusses the range of L_1, and the critical value L_{1_cri} is calculated exactly.

The design procedure and an example are given in Section 7. The experimental results obtained on a 60 W prototype are presented.

2. Mechanism of Short Current

As shown in Figure 1, the voltage source E_{in} and large DC inductor L_{DC} comprise a quasi-current source. Two switching pairs (S1/S4 and S2/S3) operate complementarily to inject a square wave current into the parallel resonant tank (composed of L_P and C_P). When the operating frequency f_S equals f_{ZVS}, the switching instants are accurate on the zero crossing point of the resonant voltage u_{C_P}. The corresponding waveform and circuit are illustrated in Figure 3.

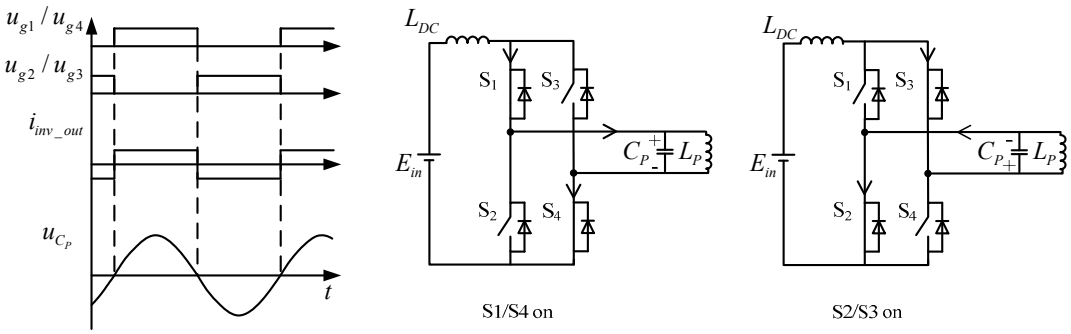

Figure 3. Waveform and circuit when f_S equals to f_{ZVS}.

For the resonant network, ZVS frequency f_{ZVS} is close to the zero phase angle resonant frequency f_r [9,11]. Because f_r is easier to calculate than f_{ZVS}, f_{ZVS} can be replaced by f_r in the following analysis. f_r is calculated by:

$$Angle[Z_{in}(f_r)] = 0 \tag{1}$$

As illustrated in Figure 1, Z_{in} is the input impedance of the resonant network under the operation frequency f_S. Therefore, when f_S equals f_r, the resonant network is purely resistant and the short current is eliminated. If f_S drifts away from f_r, a frequency drift will happen, and a short current will be generated. According to the different loops of short current, short currents can be divided into two types:

A. Capacitive case, $Angle[Z_{in}(f_s)] < 0$

In this case, the resonant network is resistive-capacitive ($Angle[Z_{in}(f_s)] < 0$) when f_S drifts away from f_r. The AC input voltage u_{C_P} is lagging the fundamental harmonic of the AC input current i_{inv_out}. When i_{inv_out} reverses its direction, u_{C_P} has not reached its zero point. The change of switches' state generates a path to short C_P. As a result, the generated short current is extremely high. The instantaneous short current may damage the switch devices. This is shown in Figure 4a.

Generally, the resonant network is resistant-capacitive when f_S is higher than f_r, since a parallel network is used on the primary side. This case is called "higher case".

B. Inductive case, $Angle[Z_{in}(f_s)] > 0$

Meanwhile, in the inductive case, the resonant network is resistive-capacitive ($Angle[Z_{in}(f_s)] > 0$) when f_S deviates from f_r. The AC input voltage u_{C_P} is led to the fundamental harmonic of the AC input current i_{inv_out}. When u_{C_P} reaches its zero point, i_{inv_out} has not reversed its direction. A loop is generated to clamp u_{C_P} to 0 V. The short current will be clamped to track the current (flowing in L_P). The waveform and short circuit in this case are shown in Figure 4b.

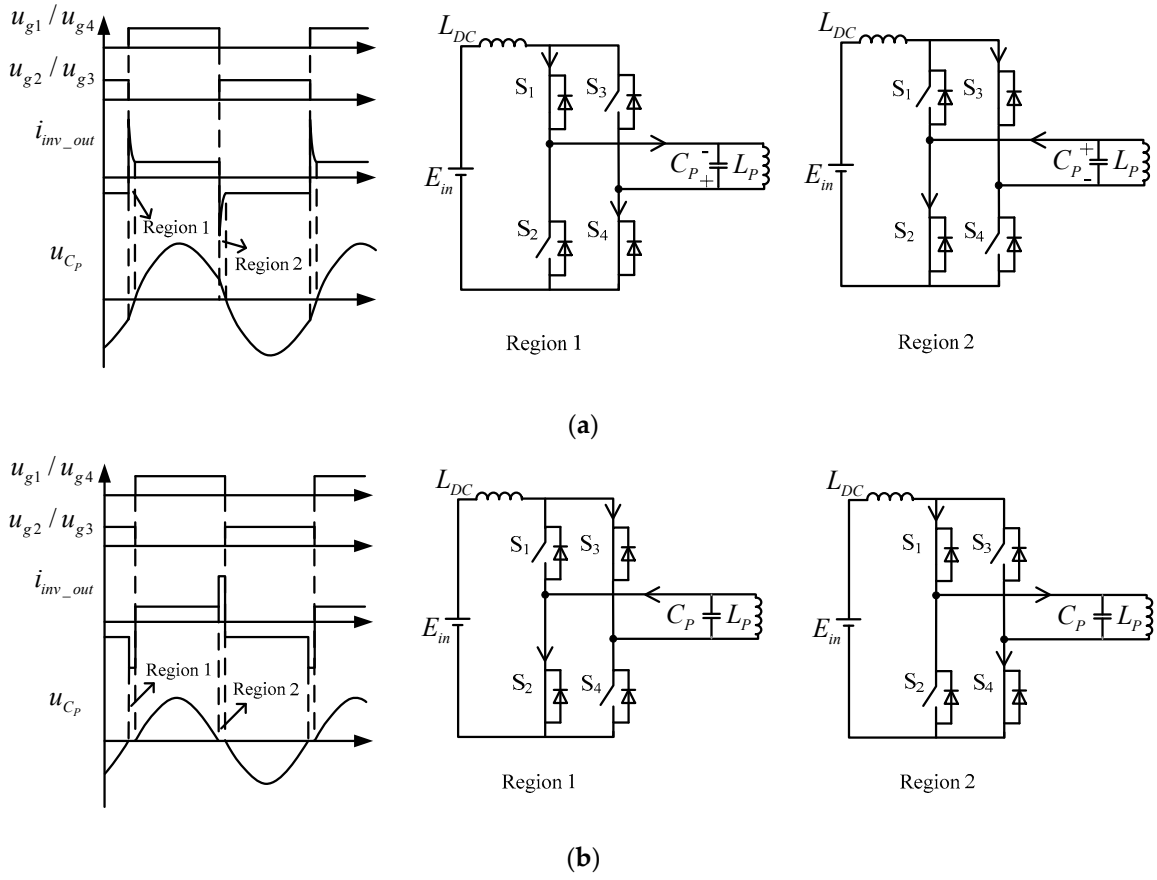

Figure 4. Short current analysis in a Current-Fed IPT system: (**a**) Capacitive case, $f_S > f_r$; (**b**) Inductive case, $f_S < f_r$.

Generally, the resonant network is resistant-inductive when f_S is lower than f_r. This case is called "lower case" in [16]. From the above analysis, a criterion is proposed to eliminate short currents in circuits that have the same topology as Figure 2:

When $u_{C_P} > 0$, S2 and S3 must remain in an off state.
When $u_{C_P} < 0$, S1 and S4 must remain in an off state.

If the criterion is broken, a short current will appear. Comparing the two cases, the capacitive case is more dangerous to the switching devices because short current in this case is uncontrollable. The inductive case is relatively safe because the short current can be clamped to a certain value (the current flowing in L_P).

3. The Proposed Inductance-Damping Method

Figure 5 shows a typical current-fed WPT system topology with the proposed inductance-damping method. Inductor L_1 is connected in series with the resonant network. L_1 is placed in the loop of the short current and will dampen any high di/dt ratio generated by a short current.

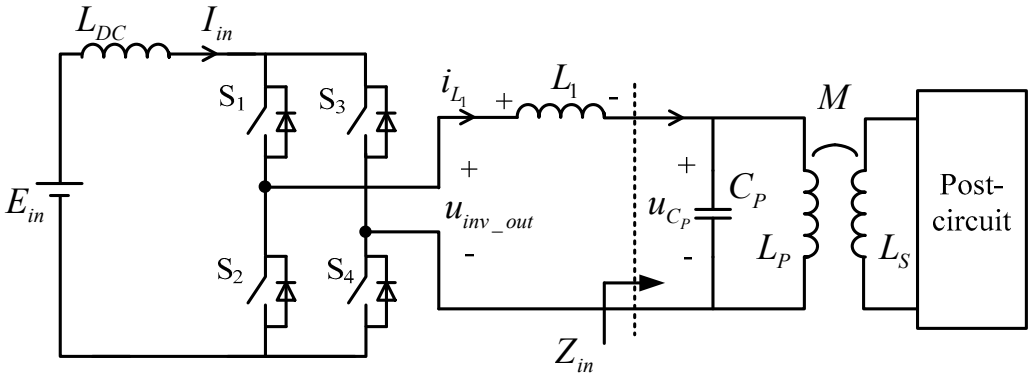

Figure 5. Current-Fed WPT system using the proposed inductance-damping method.

On the primary side, the topology of the proposed circuit is similar to a LCL network, but it works in an absolutely different way. In an LCL network, L_1 is a resonant component. However, in the proposed circuit, L_1 is not a resonant component. It is used to smooth the short current during the commutation period During the other switching cycle periods, it undertakes the DC current I_{in}.

Figure 6 shows the theoretical waveform of the circuit over a steady-state cycle. S1 and S4 are switched with the same pulse, while S3 and S4 are switched with the other pulse. Turn-on signals of S1/S4 and S2/S3 have a phase difference of 180°.

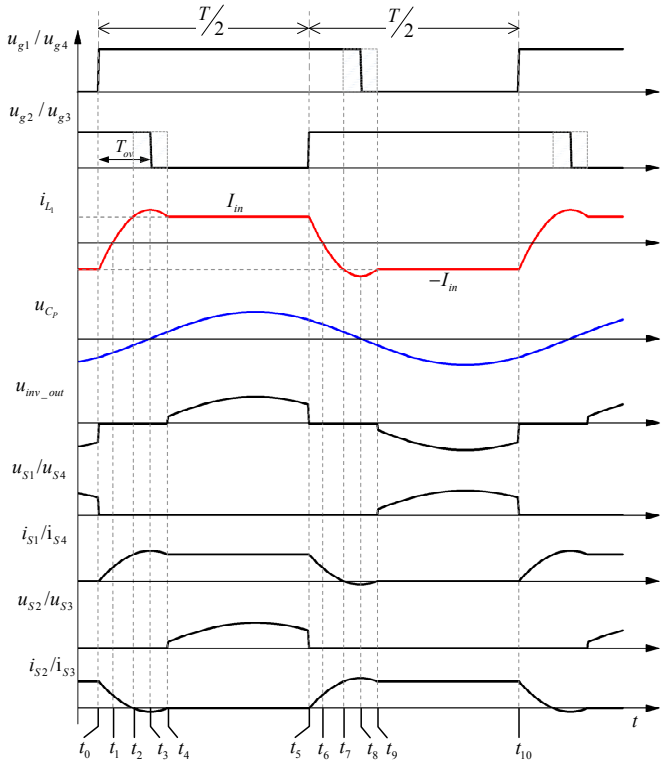

Figure 6. Steady-state waveform of the proposed system in a cycle.

Compared with the PWM pulse in Section 2, the turn-off signals of S1/S4 and S2/S3 are delayed by T_{ov}. That is, an overlap time T_{ov} is added to the PWM sequence, which means each switch is in the on state during the period. In addition, to guarantee the generation of a short current in the capacitive case, the frequency of the PWM frequency f_S must satisfy :

$$Angle[Z_{in}(f_S)] < 0 \tag{2}$$

Generally, f_S need to be higher than f_r to satisfy (2). Since operation and the waveform under steady state conditions are symmetrical in every half cycle, the equivalent circuit of every operation mode between t_0 and t_5 is illustrated in Figure 7.

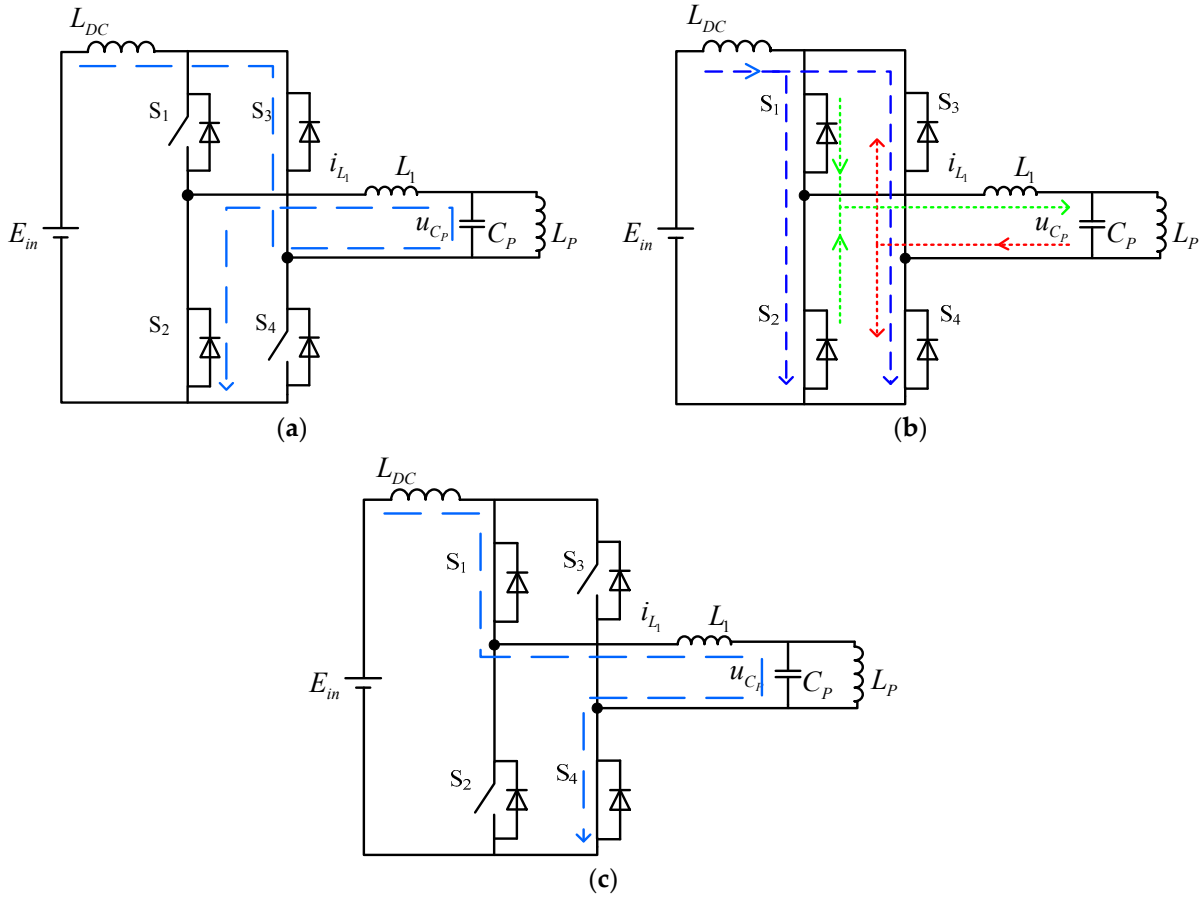

Figure 7. Operating modes of the proposed system: (**a**) Mode 0 [Before t_0]; (**b**) Mode 1 [$t_0 - t_4$]; (**c**) Mode 2 [$t_4 - t_5$].

Normally due to the frequency selection ability of the resonant network, the voltage of C_P can be considered as its fundamental component. When t_0 is selected as the origin of a cycle, u_{C_P} can be represented as:

$$u_{C_P}(t) = V_{C_P\_m} \sin(\omega t - \omega t_3) \tag{3}$$

where $\omega = 2\pi f_S$.

A. Mode 0: Before t_0, Figure 7a

In the mode, S2 and S3 are in the on state, S1 and S4 are in the off state. The voltage of S1 and S4 is equal to the absolute value of u_{C_P}. The current flowing through L_1 (i_{L_1}) is equal to $-I_{in}$.

B. Mode 1: $t_0 - t_4$, Figure 7b, Overlapping Period/Commutation Period

In this mode, i_{L_1} changes its direction smoothly, and no voltage spike is generated. At t_0, S1 and S4 turn on, and the four switches are all on. This means the resonant network and power supply are in the short mode. C_P is connected in parallel with L_1. So:

$$\begin{aligned} u_{inv\_out} &= 0 \\ u_{L_1}(t) &= L_1 \frac{di_{L_1}(t)}{dt} = -u_{C_P}(t) \end{aligned} \tag{4}$$

Because u_{C_P} is negative, the current of L_1 starts to increase from $-I_{in}$ to positive:

$$i_{L_1}(t) = \int_{t_0}^{t} \frac{-u_{C_P}(t)}{L_1} \cdot dt - I_{in} = V_{C_P\_m} \frac{\cos(\omega t - \omega t_3) - \cos(-\omega t_3)}{\omega L_1} - I_{in} \tag{5}$$

In the mode, the current flowing in each switch is the combination of the input current I_{in} and short current i_{L_1}. We have:

$$\begin{aligned} i_{S1} = i_{S4} &= \tfrac{I_{in}}{2} + \tfrac{i_{L_1}}{2} \\ i_{S2} = i_{S3} &= \tfrac{I_{in}}{2} - \tfrac{i_{L_1}}{2} \end{aligned} \tag{6}$$

As can be seen in Figure 6, current flows through S1 and S4, i_{S1}/i_{S4} increases from 0 to positive gradually after t_0. Therefore, S1 and S4 turn on with ZCS.

At t_1, i_{L_1} crosses the zero point.

At t_2, i_{L_1} increases to I_{in}, and i_{S2}/i_{S3} decreases to 0. After t_2, i_{L_1} is higher than I_{in}. It means i_{S2}/i_{S3} is reversed to negative.

At t_3, u_{C_P} is equal to 0, i_{L_1} reaches its peak and starts to decrease:

$$i_{L_1\_m} = i_{L_1}(t_3) = V_{C_P\_m} \frac{1 - \cos(-\omega t_3)}{\omega L_1} - I_{in} \tag{7}$$

At t_4, i_{L_1} decreases to I_{in}, and S2/S3's anti-parallel diodes turn off.

When S2 and S3 turn off between t_2 and t_4, the reversed i_{S2}/i_{S3} current will flow through their anti-parallel diodes. As a result, S2 and S3 can turn off with ZVS, so the switches' overlap time T_{ov} should satisfy:

$$(t_2 - t_0) < T_{ov} < (t_4 - t_0) \tag{8}$$

C. Mode 2: $t_4 - t_5$, Figure 7c, Energy-input Period

In this mode, i_{L_1} is equal to the input current I_{in} and stays constant. Considering the inductor L_1 is usually designed small, u_{inv_out} is nearly equal to u_{C_P}. Thus energy from E_{in} is input to the resonant network. Operation in the remaining half switching cycle is symmetrical to the previous four operation modes. Therefore, the four switches S1–S4 can all turn on with ZCS and turn off with ZVS.

4. Steady-State Analysis and Operation Conditions

4.1. Steady-State Analysis

Because of the high order and resonant characteristics, the accurate steady state model becomes extremely complex and is not suitable for design. The paper proposes an approximate modeling method by ignoring the short overlap time in a cycle. The detailed analysis is as follows:

Since u_{C_P} can be considered as a standard sinusoid, the system can be divided into two parts, the switching network and the resonant network. As illustrated in Figure 8, for the switching part, the post-circuit can be regarded as an AC load u_{C_P}; for the resonant part, the pre-circuit can be regarded as an AC source u_{C_P}.

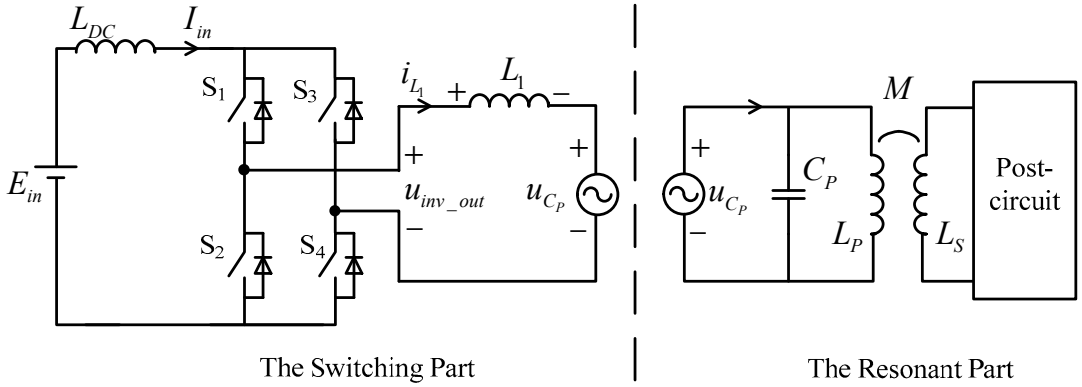

Figure 8. Equivalent circuit for steady-state analysis.

As shown in Figure 6, during the first half cycle, u_{inv_out} can be written as:

$$u_{inv\_out} = \begin{cases} 0 & t_0 \le t < t_4 \\ V_{C_P\_m} \sin(\omega t - \omega t_3) & t_4 \le t \le t_5 \end{cases} \tag{9}$$

Output power of power supply can be derived:

$$P_{\text{supple\_in}} = E_{in} \cdot I_{\text{in}} \tag{10}$$

Output power of inverter is:

$$\begin{aligned} P_{inv\_out} &= \frac{2}{T}\int_{t_0}^{t_5} i_{L_1} u_{inv\_out} \cdot dt = \frac{2}{T}\int_{t_4}^{t_5} I_{in} V_{C_P\_m} \sin(\omega t - \omega t_3) \cdot d\theta \\ &= \frac{1}{\pi} I_{in} V_{C_P\_m} \cdot [\cos(\omega t_4 - \omega t_3) - \cos(\pi - \omega t_3)] \end{aligned} \tag{11}$$

Considering that most of the power is transferred by the fundamental harmonics, the input power of resonant network can be derived:

$$P_{res\_in} = \frac{V_{Cp\_m}^2}{2} \cdot \frac{\cos\theta}{|Z_{in}|} \tag{12}$$

Phase difference θ between u_{inv_out} and fundamental harmonic of i_{L_1} is the same as the impedance angle of resonant network (Z_{in}):

$$Z_{in} = \left(j\omega L_P + \frac{\omega^2 M^2}{Z_S}\right) // \frac{1}{j\omega C_P} = \frac{1}{\frac{1}{\left(j\omega L_P + \frac{\omega^2 M^2}{Z_S}\right)} + j\omega C_P} \tag{13}$$

In (13), Z_S is the impedance of circuit in secondary side, which is relative to the resonant network and load. Compared with the switching period T, the short overlap time between t_0 and t_4 can be ignored. Thus, $t_3 \approx t_4 \approx 0$, (11) and (12) can be simplified:

$$P_{inv\_out} = \frac{2}{\pi} I_{in} V_{C_P\_m} \tag{14}$$

Ignoring the loss of L_{DC}, inverter and L_1, we have:

$$P_{\text{supple\_in}} = P_{inv\_out} = P_{res\_in} \tag{15}$$

Using (10), (12), (14) and (15), we have:

$$I_{in} = \frac{\pi^2 E_{in}}{8} \frac{\cos\theta}{|Z_{in}|} \tag{16}$$

$$V_{C_{P\_m}} = \frac{\pi}{2} E_{in} \tag{17}$$

$$P_{res\_in} = \frac{\pi^2 E_{in}^2}{8} \cdot \frac{\cos\theta}{|Z_{in}|} \tag{18}$$

Equations (17) and (18) can be used to consider the voltage and current stress of switches and passive components. Equation (19) can be used to approximately calculate the power that is transferred to the load.

4.2. DC Voltage Gain

In the system, input-output voltage gain (G_v) can be divided into two parts: voltage gain of the inverter and voltage gain of the rest circuit. Voltage gain of the inverter is derived by:

$$G_{v1} = \frac{V_{C_{P\_m}}}{E_{in}} = \frac{\pi}{\cos(\omega t_4 - \omega t_3) - \cos(\pi - \omega t_3)} \tag{19}$$

When t_3 and t_4 are small enough, (19) is simplified:

$$G_{v1} = \frac{\pi}{2} \tag{20}$$

Voltage gain of the rest circuit is related to the circuit in secondary side. In Section 7, input-output voltage gain of the experimental system is derived.

4.3. Operation Condition

In order to achieve the expected operation in the proposed circuit, three conditions need to be guaranteed.

4.3.1. Operation Frequency f_S

Since the proposed method in the paper is applied to reduce the short current in the capacitive case, Z_{in} must be resistive-capacitive. Thus, f_S needs to satisfy (2) under all load and all mutual inductance conditions, from rated load to light load and from rated coupling to lighter coupling. Generally, when f_S is higher than f_r, Equation (2) is satisfied.

If Z_{in} is resistive-inductive (generally when $f_S < f_r$), the peak value of short current will be suppressed in this situation because of the damping of L_1. However, switches will sustain high voltage spikes during the switching time to change the direction of i_{L_1}, so this is not a normal operation mode.

4.3.2. Duty Ratio of PWM Pulses

S2 and S3 must turn off between t_2 and t_4 to guarantee ZVS running. That is, the two switches needs to turn off during the period when i_{L_1} is higher than I_{in}. The duty ratio of PWM pulses need to satisfy:

$$\begin{gathered} D = 0.5 + \frac{T_{ov}}{T} \\ 0.5 + \frac{t_2 - t_0}{T} < D < 0.5 + \frac{t_4 - t_0}{T} \end{gathered} \tag{21}$$

It is complex to calculate the exact value of $t_2 - t_0$ and $t_4 - t_0$ because the system is under resonant state. Moreover, when load and mutual inductance vary, $t_2 - t_0$ and $t_4 - t_0$ are changed. It means the final D needs to satisfy (21) under all load and mutual inductance condition. A simple strategy is used to satisfy the condition in all load and inductance conditions, which is carefully described in Section 5.

4.3.3. Value of L_1

Peak value of i_{L_1} must be higher than input current I_{in} to guarantee that the two switches turn off with ZVS. If L_1 is too large, the peak value of i_{L_1} during the commutation period is lower than I_{in}. In the case, i_{L_1} has to hop from a value to I_{in} in the turn-off transition of the two switches. Large voltage spikes are imposed on the switches. Figure 9 shows system's waveforms in this situation. Fortunately, because of the existence of the Collector-to-Emitter capacitor C_{CE} in switches and junction capacitors in their anti-parallel diodes, the peak value of the voltage will be suppressed. This is because the parasite capacitor can absorb the high voltage spike and make the voltage transient smoother. The critical value of L_1 is calculated in Section 6.

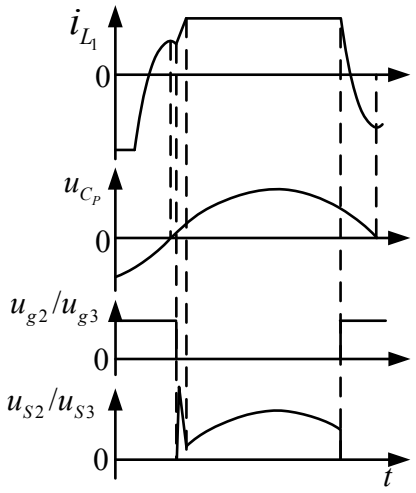

Figure 9. Waveform when L_1 is too large.

If the above conditions are satisfied, the short current can be dumped and switch voltage spike he will be eliminated.

5. Overlapping Time Self-Regulating Circuit

The turn-off time of the two on-state switches must happen between t_2 and t_4 to satisfy the second condition listed in Section 4. An automatic overlapping-time regulator is proposed to guarantee the turn-off time happens between t_2 and t_4. Because $|t_2 - t_0|$ and $|t_4 - t_0|$ is short (usually below 1 μs), the regulating circuit should be extremely fast.

In this paper, a simple but effective implement is fabricated based on the principle pointed in Section 3. When i_{L_1} reach its peak at t_3, u_{C_P} will definitely cross its zero point, and t_3 must be between t_2 and t_4. If the switch can turn off at the moment when u_{C_P} crosses the zero point, soft commutation can be achieved. In implementation, only a high-speed zero-crossing comparator is needed to detect the moment when u_{C_P} crosses the zero point. The implementation diagram that automatically regulates the overlapping-time is shown in Figure 10.

Considering time delay in the zero-crossing comparator and driver, a phase-lead compensator is used to compensate the time delay. Two phase-lead networks are generally used in practice [18], which is also shown in Figure 10. Network 1 is used in the experimental circuit to compensate the time delay.

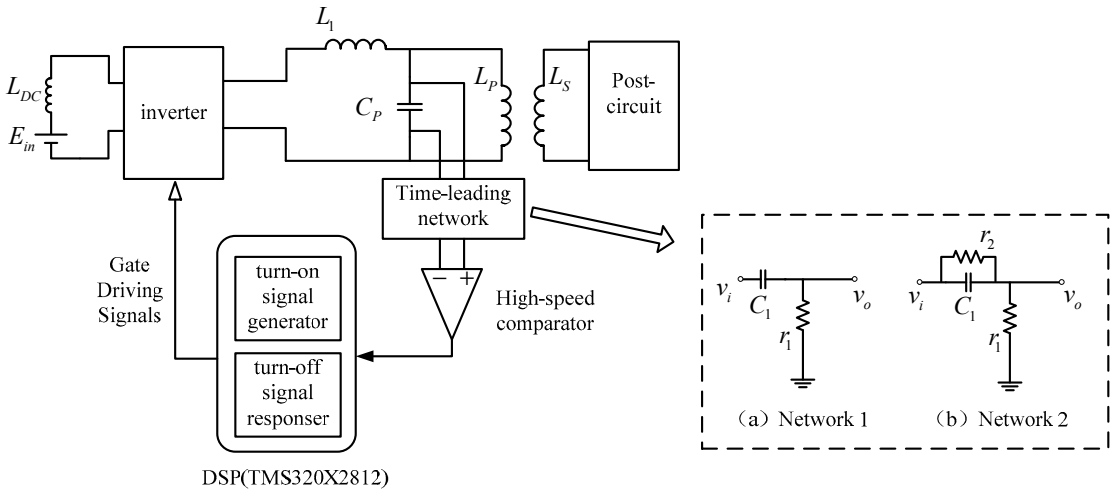

Figure 10. Schematic diagram of overlapping-time self-regulating circuit.

6. Range of L_1 and the Critical Value

In the proposed system, L_1 is an important circuit component. The value of L_1 must be considered carefully. During the commutation period, if L_1 is too large, the peak value of i_{L_1} is lower than I_{in} and soft commutation fails. If L_1 is too small, the peak value of i_{L_1} is too high to damp the short current. Therefore, the range of L_1 needs to be ascertained, and the boundary value of L_1 needs to be calculated exactly. The proper value of L_1 needs to be considered based on that.

A special operation situation (the critical mode) of the system is observed and used to confirm range of L_1.In the critical mode, peak value of i_{L_1} equals to I_{in}. Value of L_1 in this situation is the boundary value of L_1—called L_{1_cri}. Waveform of the critical mode is shown in Figure 11.

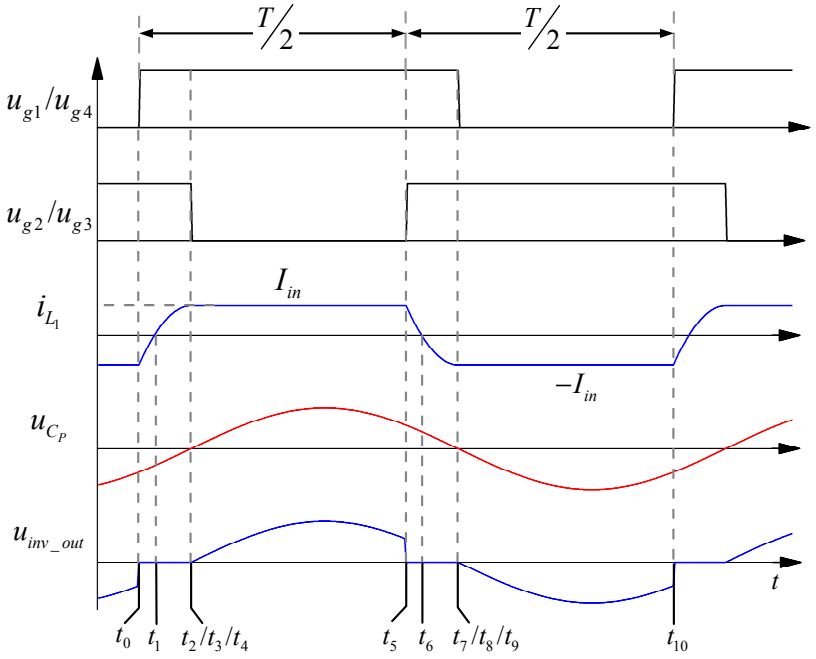

Figure 11. Waveform in the critical mode.

In the critical mode, $t_2 = t_3 = t_4$.

i_{L_1} during the commutation period is derived by:

$$\begin{aligned} u_{L_1}(t) &= -u_{C_P}(t) = L_{1\_cri}\frac{di_{L_1}(t)}{dt} \\ i_{L_1}(t) &= \int_{t_0}^{t}\frac{-u_{C_P}(t)}{L_{1\_cri}}\cdot dt - I_{in} = V_{C_P\_m}\frac{\cos(\omega t-\omega t_3)-\cos(-\omega t_3)}{\omega L_{1\_cri}} - I_{in} \end{aligned} \tag{22}$$

At t_3, u_{C_P} is equal to zero and i_{L_1} reaches its peak value:

$$i_{L_1\_m} = V_{C_P\_m}\frac{1-\cos(\omega t_3)}{\omega L_1} - I_{in} = I_{in} \tag{23}$$

During the first half cycle, i_{L_1} can be written as:

$$i_{L_1}(t) = \begin{cases} V_{C_P\_m}\frac{\cos(\omega t-\omega t_3)-1}{\omega L_{1\_cri}} + I_{in} & 0 \le t < t_3 \\ I_{in} & t_3 \le t \le t_5 \end{cases} \tag{24}$$

In the second half cycle, i_{L_1} is the negative value of the first half cycle. So the fundamental component of i_{L_1} ($i_{L_1,fun}$) is derived by Fourier series, we have:

$$\begin{aligned} &i_{L_1,fun} = A\cos\omega t + B\sin\omega t = \sqrt{A^2+B^2}\sin(\omega t+\varphi) \\ &A = \tfrac{4}{T}\textstyle\int_0^{\frac{T}{2}} i_{L_1}\cos\omega t\cdot dt \\ &B = \tfrac{4}{T}\textstyle\int_0^{\frac{T}{2}} i_{L_1}\sin\omega t\cdot dt \\ &\tan\varphi = \tfrac{A}{B} \end{aligned} \tag{25}$$

φ is the phase angle of $i_{L_1,fun}$, which takes t_0 as a reference.
Then we have:

$$\begin{aligned} Angle[u_{C_P}] - Angle[i_{L_1,fun}] &= Angle[Z_{in}] \\ \omega t_3 - \varphi &= \theta \end{aligned} \tag{26}$$

In the mode, (11) is simplified:

$$P_{inv\_out} = \frac{1}{\pi}I_{in}V_{C_P\_m}\cdot[1+\cos(\omega t_3)] \tag{27}$$

Equations (15) and (27) make up a simultaneous equation set. Thus, L_{1_cri}, t_3 and V_{Cp_m} can be calculated by a numerical algorithm simultaneously.

L_1 must be lower then to satisfy the third operation condition, so we have:

$$L_1 < L_{1\_cri} \tag{28}$$

A value of L_1 that is slightly lower than L_{1_cri} is suitable, since the operation conditions are satisfied while performance of the proposed method is guaranteed.

7. Design Procedure, Example and Measurements

7.1. Design Flowchart

When applying the proposed method to a traditional Current-Fed IPT system, f_S and L_1 need to be considered. The criterion of choosing f_S and L_1 is that the system must operate normally when resonant components and loads vary. The design procedure is shown in Figure 12.

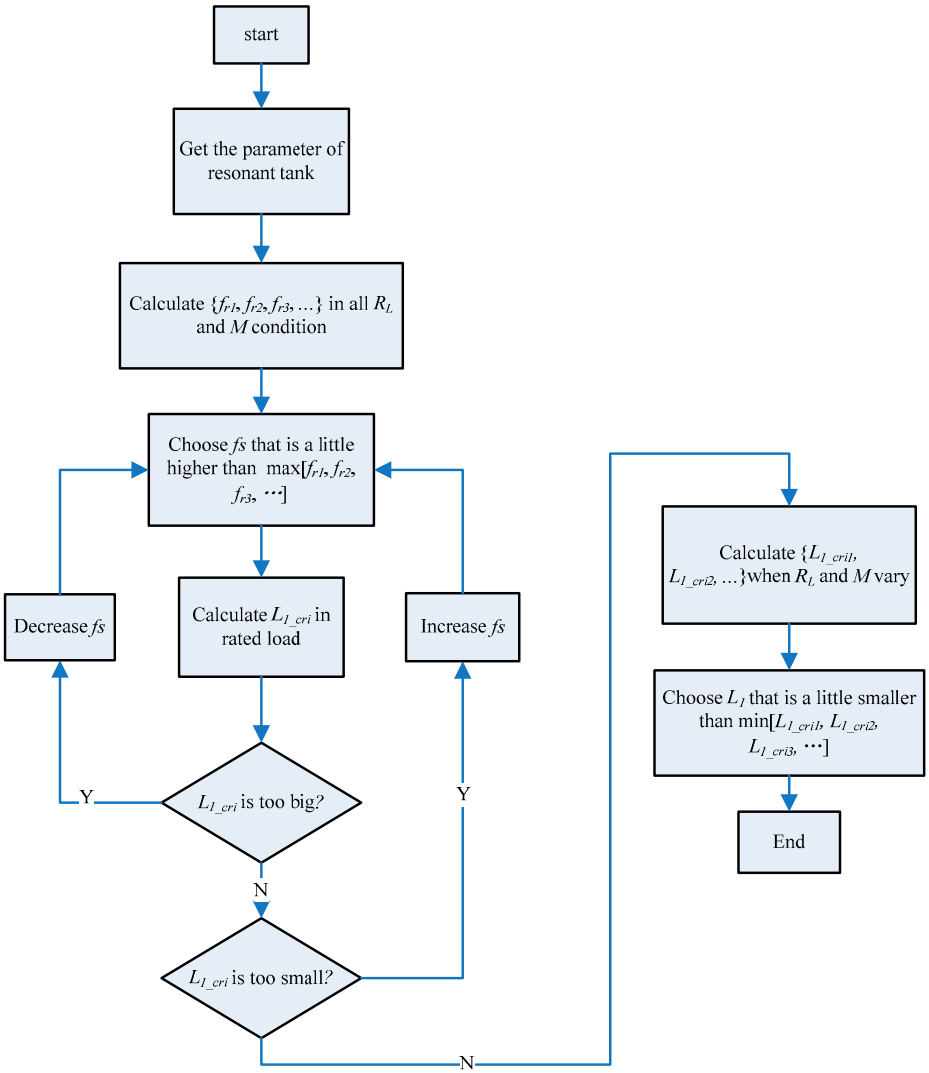

Figure 12. Design flowchart.

7.2. Design Example

A 60 W experimental system was built using the proposed method. Its parameters are listed in Table 1. The new system is designed using the strategy in Figure 12.

Table 1. Parameters of the experimental system.

Parameter	Value
E_{in}	60 V
L_{DC}	2.23 mH
R_{LDC}	0.19 Ω
L_P	29.89 μH
R_{LP}	0.058 Ω
C_P	0.528 μF
M	11.53 μH (rated)
L_S	60.59 μH
R_{LS}	0.093 Ω
C_S	0.37 μF
C_O	220 μF
R_L	10 Ω (rated)

In the experimental system, the series network used on the secondary side is taken as an example, as illustrated in Figure 13. It must be mentioned that application of the proposed method is irrelevant to the type of network used on the secondary side. Moreover, the type of network on the secondary side is irrelevant to the analysis approach and design methodology.

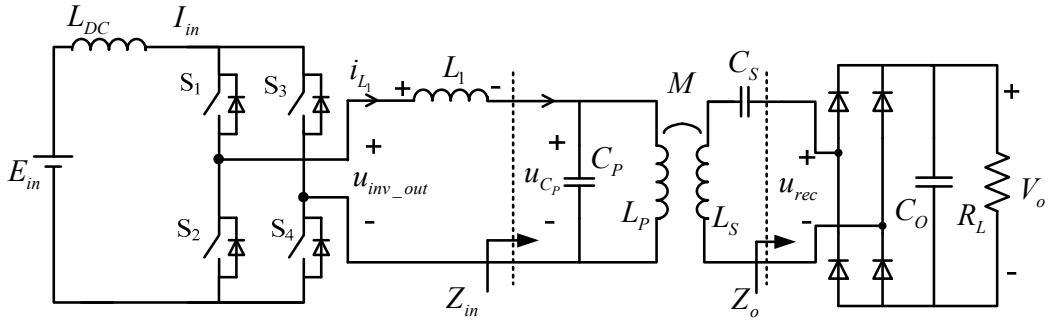

Figure 13. Circuit of the experimental system (with series resonant network in secondary side).

In the circuit:

$$Z_S = j\omega L_S + \frac{1}{j\omega C_S} + Z_o \tag{29}$$

Z_o is the equivalent AC impedance of the rectifier and its post-circuit, which can also be regarded as the AC equivalent AC load of the system. Generally, the equivalent load is considered to be purely resistant, and Z_o is calculated by:

$$Z_o = \frac{8}{\pi^2} R_L \tag{30}$$

The input-output voltage gain (G_v) of the experimental system can be divided into three parts: voltage gain of the inverter, voltage gain of the resonant network and voltage gain of rectifier. Voltage gain of inverter has been given in (20). Voltage gain of the resonant network is derived by:

$$G_{v2} = \frac{V_{rec\_1\_m}}{V_{C_P\_m}} = \frac{j\omega M}{\left(j\omega L_P + R_{L_P}\right) + \frac{\left(j\omega L_P + R_{L_P}\right)\left(j\omega L_S + R_{L_S} + \frac{1}{j\omega C_S}\right) + \omega^2 M^2}{Z_O}} \tag{31}$$

$V_{rec\_1\_m}$ is peak value of the fundamental component of the rectifier's input voltage u_{rec}. When Z_o is large enough and R_{L_P} is small enough, Equation (33) is simplified:

$$G_{v2} = \frac{M}{L_P} \tag{32}$$

The voltage gain of the rectifier and filter is:

$$G_{v3} = \frac{V_o}{V_{ref\_1\_m}} = \frac{\pi}{4} \tag{33}$$

Thus, the voltage gain of the whole system is derived:

$$G_v = G_{v1} \cdot G_{v2} \cdot G_{v3} = \frac{\pi^2}{8} \frac{M}{L_P} \tag{34}$$

Equation (34) shows that the voltage gain of the whole system is independent of the load R_L and f_S when R_L is large enough and R_{L_P} is small enough. However, the calculation result of the above model has a big error when calculating L_{1_cri} using the equation set in Section 6. Since there exists some distortion in the secondary current i_S, the equivalent load Z_o cannot be regarded as a pure resistance

and simply calculated using Equation (30). Based on the extended fundamental frequency analysis method [19], a more accurate Z_o is derived:

$$Z_o = \frac{8L_S R_L \omega}{-j(\pi^2 - 8)R_L + L_S \pi^2 \omega} \tag{35}$$

Replacing (30) with (35), the exact value of L_{1_cri} can be obtained.

The relationship between f_S and $Angle[Z_{in}]$ of the experimental system is drawn in Figure 14. The zero phase angle resonant frequencies f_r for different loads and mutual inductance conditions are all near 40 kHz. When f_S is chosen to be higher than 40 kHz, $Angle[Z_{in}]$ are all negative under different load conditions. 41 kHz is chosen to be the operation frequency since $Angle[Z_{in}(41\text{kHz})]$ remains negative when the load changes from heavy to light (R_L increases continuously) and the mutual inductance changes from the rated coupling to loose coupling.

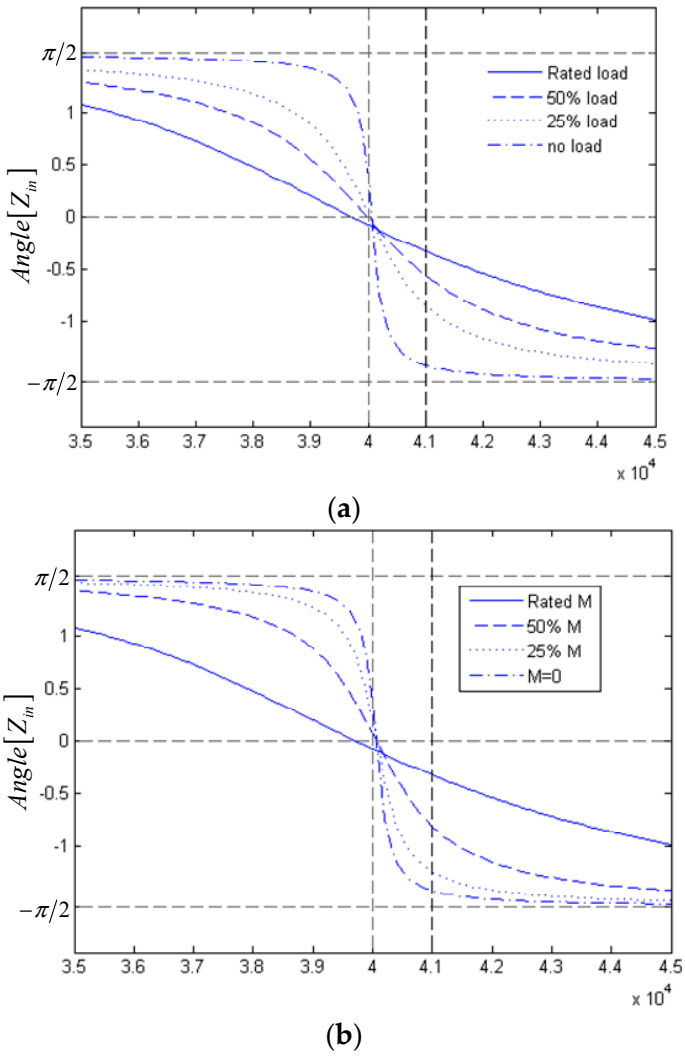

Figure 14. Relationship between $Angle[Z_{in}]$ and operating frequency of the experimental system: (**a**) R_L varies, M = 11.53 μH; (**b**) M varies, R_L = 10 Ω.

Next, the proper value of L_1 is considered. The first thing is calculating L_{1_cri} at the rated load and coupling ($R_L = 10\ \Omega$, $M = 11.53$ μH). In this case, $L_{1\_cri} = 6.86$ μH.

Then calculate L_{1_cri} when M and R_L vary. The results are shown in Figure 15. When R_L varies from rated load to light load, the correspondent L_{1_cri} increases monotonously. When the mutual inductance M varies from rated coupling to weak coupling, the corresponding L_{1_cri} increases monotonously. Therefore, if L_{1_cri} is equal to or lower than 6.87 μH, the third operating condition will be naturally achieved when R_L and M vary.

Considering the error of measurement and modeling, L_1 needs to be smaller than 6.86 μH to guarantee the third operating condition. In this experimental system, the value of L_1 is 3.85 μH.

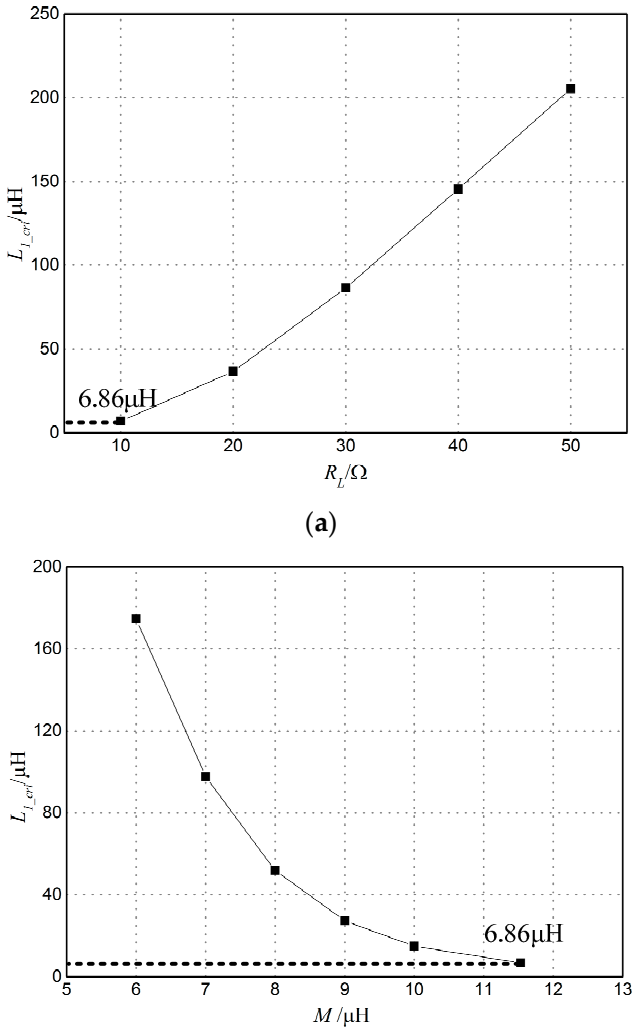

Figure 15. The critical value L_{1_cri}: (**a**) R_L varies, M = 11.53 μH; (**b**) M varies, R_L = 10 Ω.

7.3. Experiment and Performance

A proposed 60 W Current-Fed WPT prototype is built to verify the method. The experimental system is set up as shown in Figure 13. The switching components used are IGBT FGA25N120ANTD and STPS20120D diodes. The driving signals are produced by a TMS320X2812 DSP. Photos of the prototype system are shown in Figures 16 and 17.

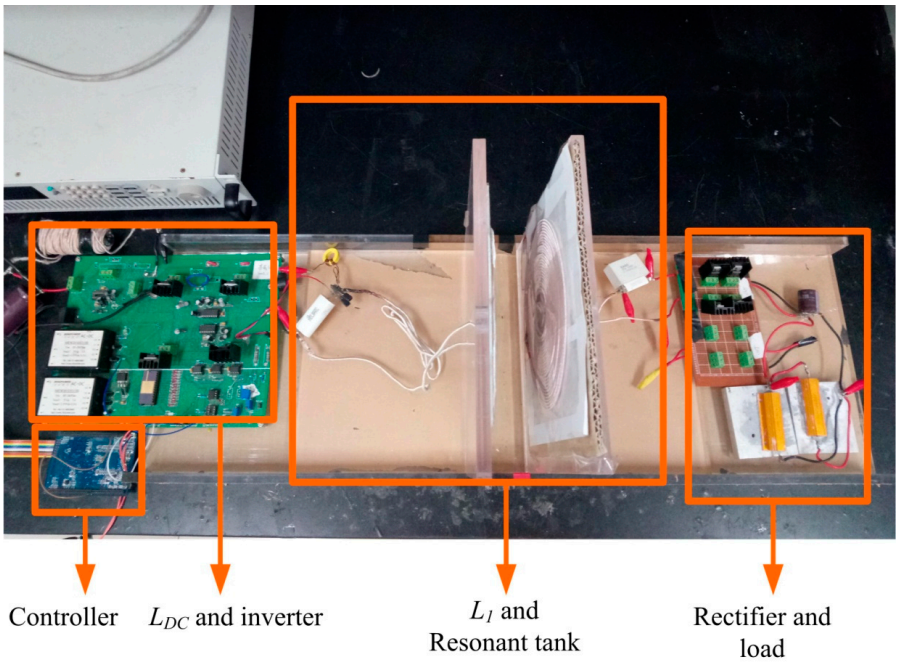

Figure 16. Photo of the prototype.

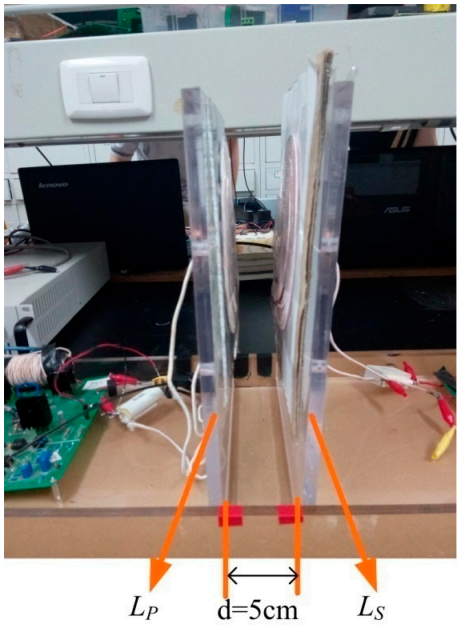

Figure 17. The coupling structure.

Figure 18 shows a comparison of the measured waveforms at rated load. Short currents are greatly damped in the system with the proposed method. The peak value of the short current in a traditional system is several times higher than I_{in}, while the short current in the system with the proposed method is kept at a very low level.

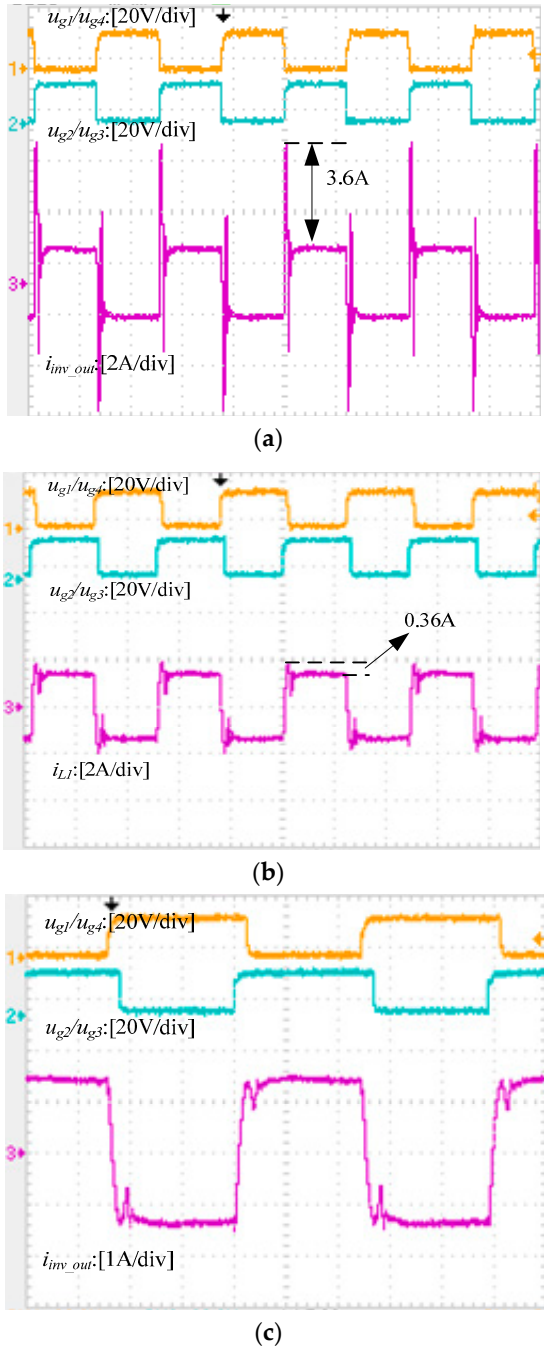

Figure 18. Short current control performance comparison: (**a**) Traditional parallel WPT system under heavy load condition (R_L = 10 Ω); (**b**) Short current control performance with L_1 = 3.45 μH, R_L = 10 Ω; (**c**) Short current control performance with L_1 = 6.40 μH, R_L = 10 Ω.

Due to parasitic capacitance in the switches and junction capacitors in their anti-parallel diode, a current oscillation exists in i_{L_1} after t4. Figure 18c illustrates the waveform of the system with the proposed approach when L_1 = 6.40 μH. In this situation, the peak value of the short current is nearly equal to I_{in}, which verifies the accuracy of the model in Section 6. As shown in Figure 18b, 3.45 μH is a proper value of L_1, so in the remaining experiments, L_1 is chosen to be 3.45 μH.

Detailed waveforms of the proposed system are shown in Figure 19. As described in Section 5, the switches turn off in the zero-crossing point of u_{Cp}. The overlap time Tov is regulated automatically and the operation conditions are satisfied.

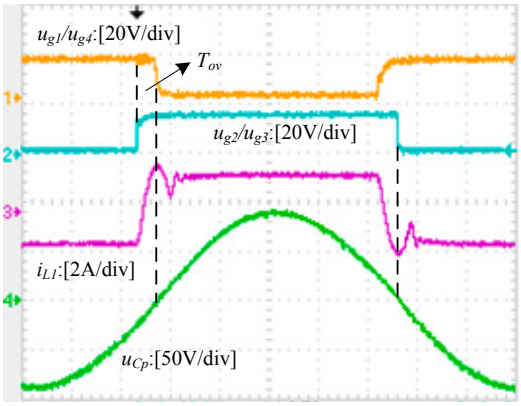

Figure 19. The switching waveform during the commutation period (when R_L = 10 Ω, L_1 = 3.45 μH).

Figure 20 shows waveforms of one switch. During the turn-on time, the current of switch i_S equals to 0 and slowly increases, which means ZCS is achieved. At turn-off time, the voltage of the switch u_{Cp} remains at zero and ZVS are achieved. Because of these excellent properties, loss of switching devices in the system can be greatly reduced, that is, the efficiency will be enhanced. When the distances of L_P and L_S increase, the system still operates normally, as shown in Figure 21.

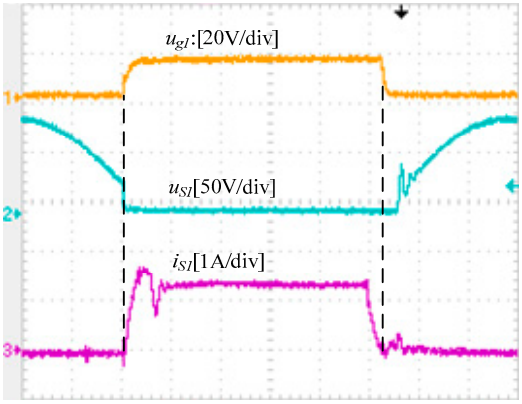

Figure 20. Waveform of switch (when R_L = 10 Ω, L_1 = 3.45 μH).

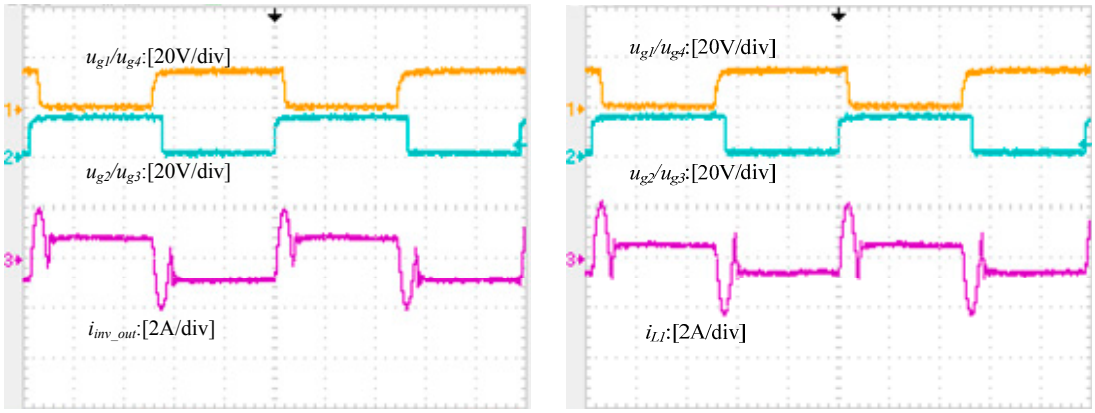

(**a**) (**b**)

Figure 21. Steady-state waveform when M varies (R_L = 10 Ω, L_1 = 3.45 μH): (**a**) 6 cm, M = 8.77 μH; (**b**) 7 cm, M = 6.70 μH.

To verify the theoretical model, a set of experimental data was measured. The experimental and theoretical voltage gains are compared in Figure 22.

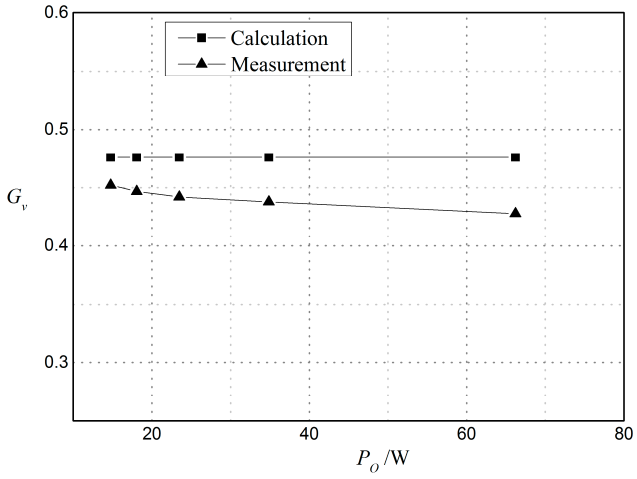

Figure 22. Comparison of theoretical value and experimental data of G_v.

The efficiency of traditional parallel WPT system and new WPT system is compared in Figure 23. During large load variation, efficiency of proposed system is always higher than traditional system due to short current is effectively controlled.

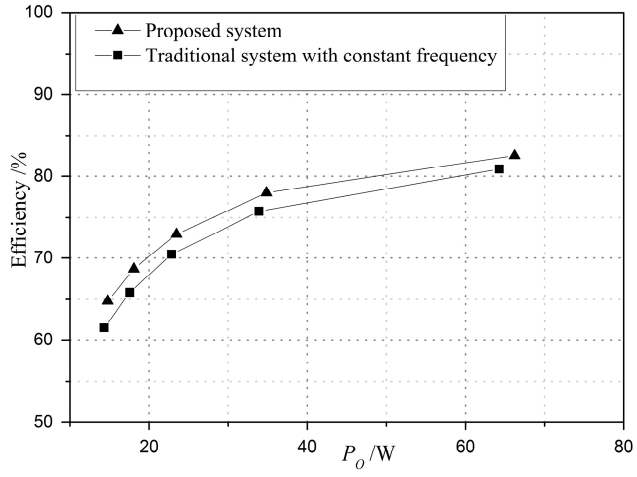

Figure 23. Efficiency of traditional system and proposed system.

8. Conclusions

Short currents occur in WPT systems when the operation frequency drifts from the inherent frequency of the resonant network. This phenomenon is quite dangerous for switching components and other circuit components. This paper proposes a novel method, named inductance-damping method, based on utilizing an additional small inductance to inhibit short currents. Steady-state mode and operating conditions are analyzed. An overlapping time regulation circuit is given and the range of G_v is discussed. The system design procedure is described and a design example is discussed. The experimental waveforms and data are given to verify the method. Furthermore, this method can be extended to Current-Fed full-resonant converters.

Acknowledgments: The research work is financially supported by the research fund of National Natural Science Foundation of China (Nos. 51377183, 51377187).

Author Contributions: Author Yanling Li implemented the research, performed the analysis, experimental data analysis and wrote the paper. Author Qichang Duan contributed the main idea of this paper and provided guidance and supervision. Author Weiyi Li carried out experimental tests.

Conflicts of Interest: The authors declare no conflict of interest.

References

1. Villa, J.L.; Sallan, J.; Osorio, J.F.S.; Llombart, A. High-misalignment tolerant compensation topology for ICPT systems. *IEEE Trans. Ind. Electron.* **2012**, *59*, 945–951. [CrossRef]
2. Zhang, W.; Wong, S.C.; Chi, K.T.; Chen, Q. Design for efficiency optimization and voltage controllability of series—Series compensated inductive power transfer systems. *IEEE Trans. Power Electron.* **2014**, *29*, 191–200. [CrossRef]
3. Pantic, Z.; Lukic, S.M. Framework and topology for active tuning of parallel compensated receivers in power transfer systems. *IEEE Trans. Power Electron.* **2012**, *27*, 4503–4513. [CrossRef]
4. Thrimawithana, D.J.; Madawala, U.K. A generalized steady-state model for bidirectional IPT systems. *IEEE Trans. Power Electron.* **2013**, *28*, 4681–4689. [CrossRef]
5. Huang, C.Y.; Boys, J.T.; Covic, G.A. LCL pickup circulating current controller for inductive power transfer systems. *IEEE Trans. Power Electron.* **2013**, *28*, 2081–2093. [CrossRef]
6. Madawala, U.K.; Neath, M.; Thrimawithana, D.J. A power–frequency controller for bidirectional inductive power transfer systems. *IEEE Trans. Ind. Electron.* **2013**, *60*, 310–317. [CrossRef]
7. Chen, R.Y.; Liang, T.J.; Chen, J.F.; Lin, R.L.; Tseng, K.C. Study and implementation of a current-fed full-bridge boost DC—DC converter with zero-current switching for high-voltage applications. *IEEE Trans. Ind. Appl.* **2008**, *44*, 1218–1226. [CrossRef]
8. Yuan, B.; Yang, X.; Zeng, X.; Duan, J.; Zhai, J.; Li, D. Analysis and design of a high step-up current-fed multiresonant DC–DC converter with low circulating energy and zero-current switching for all active switches. *IEEE Trans. Ind. Electron.* **2012**, *59*, 964–978. [CrossRef]
9. Hu, A.P. Selected Resonant Converters for IPT Power Supplies. Ph.D. Thesis, Department of Electrical and Computer Engineering, Auckland University, Auckland, New Zealand, 2001.
10. Si, P.; Hu, A.P.; Malpas, S.; Budgett, D. A frequency control method for regulating wireless power to implantable devices. *IEEE Trans. Biomed. Circuits Syst.* **2008**, *2*, 22–29. [CrossRef] [PubMed]
11. Hu, A.P.; Boys, J.T.; Covic, G.A. Frequency analysis and computation of a current-fed resonant converter for ICPT power supplies. In Proceedings of the International Conference on Power System Technology, Perth, Australia, 4–7 December 2000; pp. 327–332.
12. Tang, C.S.; Sun, Y.; Su, Y.G.; Nguang, S.K.; Hu, A.P. Determining multiple steady-state ZCS operating points of a switch-mode contactless power transfer system. *IEEE Trans. Power Electron.* **2015**, *24*, 416–425. [CrossRef]
13. Su, Y.G.; Zhang, H.Y.; Wang, Z.H.; Hu, A.P. Steady-state load identification method of inductive power transfer system based on switching capacitors. *IEEE Trans. Power Electron.* **2015**, *30*, 6349–6355. [CrossRef]
14. Wang, Z.H.; Li, Y.P.; Sun, Y.; Tang, C.S.; Lv, X. Load detection model of voltage-fed inductive power transfer system. *IEEE Trans. Power Electron.* **2013**, *28*, 5233–5243. [CrossRef]
15. Hu, A.P.; Covic, G.A.; Boys, J.T. Direct ZVS start-up of a current-fed resonant inverter. *IEEE Trans. Power Electron.* **2006**, *21*, 809–812. [CrossRef]
16. Dai, X.; Sun, Y. An accurate frequency tracking method based on short current detection for inductive power transfer system. *IEEE Trans. Ind. Electron.* **2014**, *61*, 776–783. [CrossRef]
17. Namadmalan, A. Bidirectional current-fed resonant Inverter for contactless energy transfer systems. *IEEE Trans. Ind. Electron.* **2015**, *62*, 238–245. [CrossRef]
18. Yan, K.; Chen, Q.; Hou, J.; Ren, X.; Ruan, X. Self-oscillating contactless resonant converter with phase detection contactless current transformer. *IEEE Trans. Power Electron.* **2014**, *29*, 4438–4449. [CrossRef]
19. Forsyth, A.J.; Ward, G.A.; Mollov, S.V. Extended fundamental frequency analysis of the LCC resonant converter. *IEEE Trans. Power Electron.* **2003**, *18*, 1286–1292. [CrossRef]